The Astrophysical Journal, 749:88 (13pp), 2012 April 10 doi:10.1088/0004-637X/749/1/88

THE TAIWAN ECDFS NEAR-INFRARED SURVEY: VERY BRIGHT END OF THE LUMINOSITY FUNCTION AT $z > 7$

Bau-Ching Hsieh[1], Wei-Hao Wang[1], Haojing Yan[2], Lihwai Lin[1], Hiroshi Karoji[3,4], Jeremy Lim[1,5], Paul T. P. Ho[1,6], and Chao-Wei Tsai[7]
[1] Institute of Astrophysics and Astronomy, Academia Sinica, P.O. Box 23-141, Taipei 106, Taiwan, Republic of China
[2] Department of Physics and Astronomy, University of Missouri, Columbia, MO 65211, USA
[3] National Astronomical Observatory of Japan, 2-21-1 Osawa, Mitaka, Tokyo 181-8588, Japan
[4] Institute for the Physics and Mathematics of the Universe, University of Tokyo, 5-1-5 Kashiwanoha, Kashiwa 277-8583, Japan
[5] Department of Physics, University of Hong Kong, Pokfulam Road, Hong Kong
[6] Harvard-Smithsonian Center for Astrophysics, 60 Garden Street, Cambridge, MA 02138, USA
[7] Infrared Processing and Analysis Center, California Institute of Technology, 770 South Wilson Avenue, Pasadena, CA 91125, USA
Received 2011 October 3; accepted 2012 February 7; published 2012 March 26

ABSTRACT

The primary goal of the Taiwan ECDFS Near-Infrared Survey (TENIS) is to find well-screened galaxy candidates at $z > 7$ (z' dropout) in the Extended Chandra Deep Field-South (ECDFS). To this end, TENIS provides relatively deep J and K_s data ($\sim$25.3 ABmag, 5σ) for an area of 0.5×0.5 deg. Leveraged with existing data at mid-infrared to optical wavelengths, this allows us to screen for the most luminous high-z objects, which are rare and thus require a survey over a large field to be found. We introduce new color selection criteria to select a $z > 7$ sample with minimal contaminations from low-z galaxies and Galactic cool stars; to reduce confusion in the relatively low angular resolution Infrared Array Camera (IRAC) images, we introduce a novel deconvolution method to measure the IRAC fluxes of individual sources. Illustrating perhaps the effectiveness at which we screen out interlopers, we find only one $z > 7$ candidate, TENIS-ZD1. The candidate has a weighted $z_{\rm phot}$ of 7.8, and its colors and luminosity indicate a young (45M years old) starburst galaxy with a stellar mass of $3.2 \times 10^{10}\,M_{\odot}$. The result matches with the observational luminosity function analysis and the semianalytic simulation result based on the Millennium Simulations, which may over predict the volume density for high-z massive galaxies. The existence of TENIS-ZD1, if confirmed spectroscopically to be at $z > 7$, therefore poses a challenge to current theoretical models for how so much mass can accumulate in a galaxy at such a high redshift.

Key words: galaxies: evolution – galaxies: formation – galaxies: high-redshift

Online-only material: color figures

1. INTRODUCTION

Finding objects at high redshifts is of fundamental importance in observational cosmology. By doing so, we are probing closer to the first galaxies and black holes in the universe, and therefore ever closer to the initial conditions for the formation of galaxies and structures. At the present time, we do not know when galaxies first formed, nor how quickly they can grow in mass during their extreme youth. Because $z \sim 7$ is the epoch that marks the end of the reionization, finding objects at $z > 7$ will provide crucial constraints on the source of ionizing photons, as well as in the early assembly history of galaxies and black holes.

The last decade or so has bore witness to an explosive growth in the discovery of galaxies or galaxy candidates at $z \sim$ 6–10, pushing our understanding of galaxy formation to ever earlier epochs after the Big Bang. Many efforts have been made using various techniques (e.g., Taniguchi et al. 2005; Kashikawa et al. 2006; Iye et al. 2006; Shimasaku et al. 2006; Stark et al. 2007; Mannucci et al. 2007; Ota et al. 2008, 2010; Richard et al. 2008; Bouwens et al. 2008, 2009a, 2010b, 2010a, 2010c; Oesch et al. 2009, 2010b, 2010a; Castellano et al. 2010; McLure et al. 2009, 2010, 2011; Bunker et al. 2010; Hickey et al. 2010; Henry et al. 2007, 2008, 2009; Bradley et al. 2008; Zheng et al. 2009; Capak et al. 2011; Wilkins et al. 2010, 2011; Sobral et al. 2009; González et al. 2010; Ouchi et al. 2009, 2010; Yan et al. 2011; Trenti et al. 2011, 2012), but all can be roughly separated into three categories: (1) ground-based narrowband imaging searches for Lyα emitters (LAEs), (2) space-based (*HST*/WFC3) ultra-deep narrow-field surveys for Lyman break galaxies (LBGs), and (3) ground-based deep and wide-field surveys for LBGs. The continuum emissions of the LAEs provided by category (1) are usually too faint to be detected even photometrically, and so their UV star formation rate (SFR) and the continuum luminosity function (LF) of these objects cannot be derived. After *HST*/WFC3 was launched, the sample size of category (2) increased rapidly and now dominates the $z > 6$ sample. Given the limited survey field sizes, however, these studies mainly focus on very faint samples as the probability of finding luminous but rare objects are small. By contrast, surveys corresponding to category (3) are capable of finding rare bright sources that provide the strongest leverage in constraining the bright end of the LF.

Most of the current $z > 7$ samples are provided by surveys in categories (2) and (3). The vast majority of these $z > 7$ candidates have been identified based on their photometric colors and do not have spectroscopic confirmations. Contamination by intervening objects may be severe in the currently known sample. There are two major sources of contamination, heavily reddened low-z galaxies and Galactic cool stars. For the samples provided by category (2), low-z galaxies can be well resolved by *HST*/WFC3 and so their identification is straightforward. A Galactic cool star, however, may have both similar colors and morphology as a compact galaxy at $z > 7$, and so contamination from cool stars remains an issue. Samples provided by category (3) suffer from these major contaminations. This issue has been discussed in detail in many previous studies (e.g., Ouchi et al. 2009; Capak et al. 2011), and has been recognized to be difficult

to resolve. In this paper, we use *Spitzer* Infrared Array Camera (IRAC) photometry to introduce additional criteria for significantly reducing both the above-mentioned contaminations in the category (3) studies for selecting $z > 7$ candidates.

As we utilize the *Spitzer* IRAC photometry in our analysis, we require a field with deep multi-wavelength data including *Spitzer* IRAC observations. For this purpose, the Extended Chandra Deep Field-South (ECDFS; Lehmer et al. 2005) is ideal. The ECDFS is a 0.5×0.5 deg field that surrounds both the Chandra Deep Field South (CDFS) and the Great Observatories Origins Deep Survey-South (GOODS-S) field. The ECDFS has been studied at many wavelengths in addition to the original Chandra X-ray data. In the UV, the Deep Imaging Survey for the *Galaxy Evolution Explorer* ultraviolet satellite (Martin et al. 2005) observed the entire ECDFS. In the optical, the Galaxy Evolution from Morphology and SEDs (GEMS; Rix et al. 2004; Caldwell et al. 2008) project used the Advanced Camera for Surveys (ACS) on the *Hubble Space Telescope* (*HST*) to cover nearly the entire ECDFS. The ECDFS has also been observed in many ground-based optical and near-infrared imaging projects, e.g., the Classifying Objects through Medium-Band Observations, a spectrophotometric 17-filter survey (COMBO-17; Wolf et al. 2001, optical only) program, Multiwavelength Survey by Yale-Chile (MUSYC; Gawiser et al. 2006; Taylor et al. 2009; Cardamone et al. 2010) including 10 O/NIR broad bands and 18 deep topical medium bands, and the NIR survey using ISAAC on the Very Large Telescope (VLT) in the GOODS-S field. In the infrared and far-infrared, most of the relevant data have been obtained using *Spitzer*. The *Spitzer* IRAC/MUSYC Public Legacy in the ECDFS survey (SIMPLE; Damen et al. 2011) provides deep IRAC data at wavelengths of 3.6, 4.5, 5.8, and 8.0 μm with a $10' \times 15'$ ultra-deep GOODS-S IRAC data in the center (Dickinson et al. 2003), and the Far-Infrared Deep Extragalactic Legacy survey (Dickinson et al. 2007) took MIPS images at wavelengths of 24, 70, and 160 μm to cover nearly the entire ECDFS. At radio wavelengths, the ECDFS has been covered by the VLA 1.4 GHz Survey (Kellerman et al. 2008).

As in previous surveys in category (3), we start by using the Lyman break technique to find LBGs at $z > 7$. The wavelength of the Lyman break is shifted to between z band and J band for LBGs at $z = 7$–10, i.e., LBGs at $z = 7$–10 have very red $z - J$ colors ($z - J > 2$; all the magnitudes and colors in this paper are in AB system, unless noted otherwise). Hence z-dropout objects are what we look for. In the ECDFS, the deepest available z-band data is the *HST*/ACS $F850LP$ data from the GEMS (Rix et al. 2004; Caldwell et al. 2008), which has a 5σ limiting magnitude of 27.1. To gain the full advantage of the deep $F850LP$ data, J-band data with a 5σ limiting magnitude of 25.1 are a minimal requirement. In the ECDFS, two J-band data samples are available: the GOODS-S data taken using ISAAC on the VLT and the MUSYC data. The depth of the GOODS-S J band is about 25.1 mag, which meets our requirement. The field size of the GOODS-S, however, is only about one-fifth of that of the ECDFS, significantly reducing the probability of finding rare and luminous LBGs by a factor of five. On the other hand, although the J-band data provided by the MUSYC covers the entire ECDFS, the depth is only about 23.0 mag, and thus far too shallow for finding $z > 7$ objects. A new deep ($J > 25.1$) near-infrared imaging survey with the full ECDFS coverage is therefore needed for our study.

In this paper, we describe the deep near-infrared survey that we carried out in the ECDFS, and the data reductions performed on the optical, near-infrared, and IRAC data in Section 2. In Section 3, we provide a description of the sampling criteria for this study. The possible contaminations in our sample are discussed in Section 4. We present our results and the implications of our sample in Section 5. In Section 6, we summarize our results and discuss future work. The cosmological parameters used in this study are $\Omega_\Lambda = 0.73$, $\Omega_M = 0.27$, $H_0 = 71$ km s^{-1} Mpc^{-1}, and $w = -1$.

2. DATA AND PHOTOMETRY

2.1. TENIS Data

We initiated the Taiwan ECDFS Near-Infrared Survey (TENIS) in 2007. The goal of this project is to obtain deep J and K_s images in the ECDFS, and thus fill in the big wavelength gap between 1.0 μm and 3.6 μm. TENIS is yet the deepest near-IR survey in a $30' \times 30'$ sky area with a full coverage of all four IRAC channels. Figure 1 shows the fields of the main surveys in the ECDFS: SIMPLE, GOODS-S (ACS and IRAC), MUSYC, COMBO-17, GEMS, the TENIS J, K_s, and Y. The scientific goal of the TENIS J-band observation is to search for the most luminous high-z objects (i.e., this work), which are rare and thus require a survey over a large field to be found, while the TENIS K_s-band observation is for the studies of the mass assembly history and submillimeter galaxies at $z > 2$. After combined with existing deep images in the optical and 3.6–8 μm, the TENIS data can be used to derive robust photometric redshifts and stellar masses of a large sample of galaxies. Therefore, the TENIS data set is unique not only in its depth and survey area but also in its rich multi-wavelength ancillary data in the ECDFS.

2.1.1. CFHT WIRCam Observations

The TENIS data were taken using the Wide-field InfraRed Camera (WIRCam; Puget et al. 2004) on the Canada–France–Hawaii Telescope (CFHT). WIRCam consists of four 2048×2048 HAWAII2-RG detectors covering a field of view of $20' \times 20'$ with a $0''.3$ pixel scale. To date we have spent 44 hr in J and 40 hr in K_s. The J-band data were taken in 2007B and 2008B, with an average 5σ limiting magnitude of $J = 25.5$ for point sources. The K_s-band data were taken in 2009B and 2010B, with an average 5σ limiting magnitude of $K_s = 25.0$. The average seeings were $0''.8$ and $0''.7$ for J and K_s, respectively. More details of the WIRCam imaging observations is described in the TENIS catalog paper (B.-C. Hsieh et al., in preparation).

2.1.2. Subaru MOIRCS Observation

We obtained Y data in the ECDFS using the Subaru MOIRCS in 09B. The observation is a follow-up observation of the TENIS project. The goal of the observation is to have Y-band photometry for a set of high-z objects pre-selected using their $z - J$ colors. Two pointings were planned to be observed. One is inside the GOODS-S field and the other is outside the GOODS-S field. However, due to the bad weather, only one pointing on the east side of the ECDFS was observed, i.e., a $4' \times 7'$ area outside the GOODS-S field. The 5σ limiting magnitude for point sources is 25.5. Although the Y data are only available for part of the ECDFS, the data are still very important to further improve the photometric redshift quality for the candidates in that area since the wavelength of Y band is right between those of $F850LP$ and J.

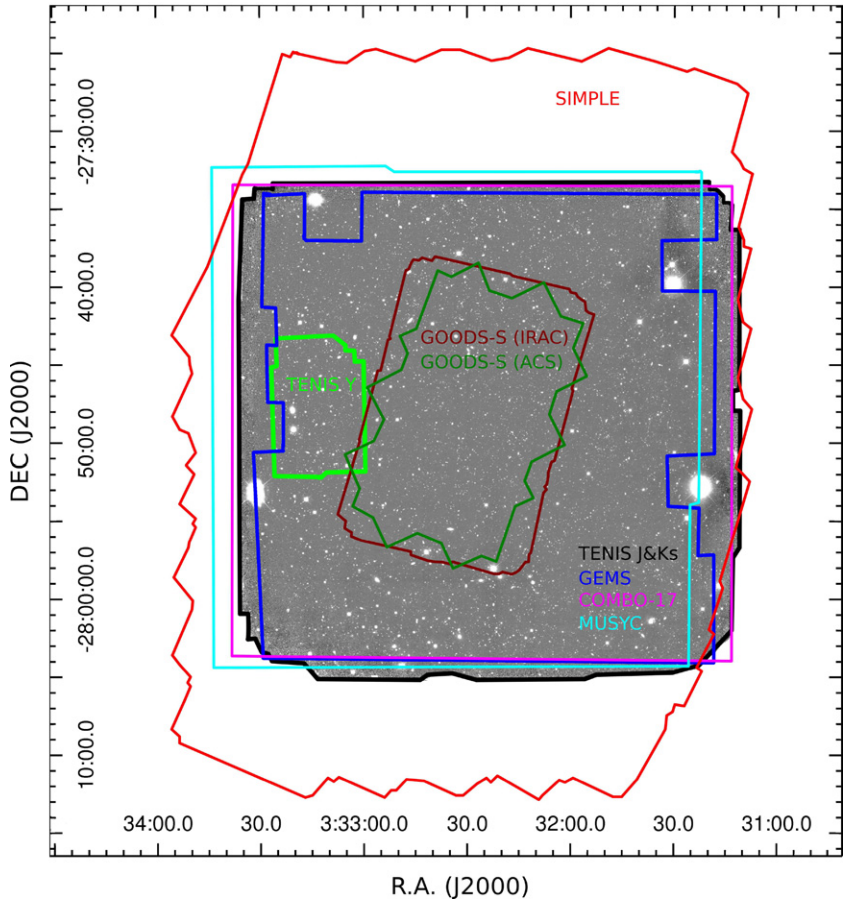

Figure 1. TENIS *J*-band image. The black lines indicate the TENIS *J*- and K_s-band fields. The green lines delineate the TENIS *Y*-band field. The blue, pink, and cyan lines indicate the fields of GEMS, COMBO-17, and MUSYC, respectively, and the GOODS-S (IRAC and ACS) fields are represented by brown and dark green lines. (A color version of this figure is available in the online journal.)

2.1.3. Data Reduction

The TENIS *J* and K_s data were processed using an Interactive Data Language based reduction pipeline called Simple Imaging and Mosaicking Pipeline. The details of the pipeline are described in Wang et al. (2010). We used the pipeline to deal with flat-fielding, removing instrumental features like crosstalk and residual images from saturated objects in previous exposures, masking satellite trails, distortion and astrometry correction, mosaicking and stacking images, and photometric calibration. The zero-point calibration was done by matching the fluxes in an aperture of 5″ in diameter with those in the Two Micron All Sky Survey point source catalogs.

2.1.4. Photometry

We used SExtractor version 2.5.0 (Bertin & Arnouts 1996) to detect objects and measure their fluxes in the WIRCam images. For the TENIS *J* image, we used the "FLUX_AUTO" values of the SExtractor output as the measured *J* fluxes. The flux errors provided by SExtractor do not include the correlated errors. Therefore, we calibrated the errors with the following procedure: first, the fluxes and the flux errors were re-measured using SExtractor with a 2″ diameter aperture. We then convolved the source-masked image with a 2″ diameter aperture and calculated the rms around each pixel on the convolved images. The ratio between the aperture photometric flux error provided by SExtractor for a certain object and the rms value around the same position in the convolved image is the correction factor of the flux error for that object. The median value of the correction factors was computed to be the general correction factor for all the sources. For *J*-band data, the general correction factor is 0.793. The same procedures were done with different aperture sizes. We find that the correction factors are very stable with different aperture sizes, which is consistent with the experience in Wang et al. (2010). Therefore, we just applied the factor to the "FLUXERR_AUTO" values for all the TENIS *J* objects to calibrate their flux errors.

For the TENIS K_s image, the double-image mode of SExtractor was performed to generate a *J*-selected K_s photometric catalog. In order to use the double-image mode, we shifted the K_s image to match to the *J* image. The K_s fluxes were also measured with the "FLUX_AUTO" option, and the flux errors were calibrated with the same procedure used in the TENIS *J* data.

To estimate the completeness for our data, we used a Monte Carlo simulation. The faint objects are compact but may not be all point-like. The medium FWHMs of objects with $J \sim 25$ is about 2.″0 ($\sim$10 kpc at $z \sim 7$). Therefore, to better determine the completeness of faint objects, we randomly put 100 artificial sources into the TENIS *J* image, with an image that is averaged from $\sim$100 real extended sources with FWHMs between 2.″0 and 2.″2, and with signal-to-noise ratios greater than 100. The magnitudes of the artificial sources are uniformly distributed in the magnitude space from 20 mag to 27 mag, and Poisson errors were added into the images of the artificial sources. We then ran SExtractor to do object

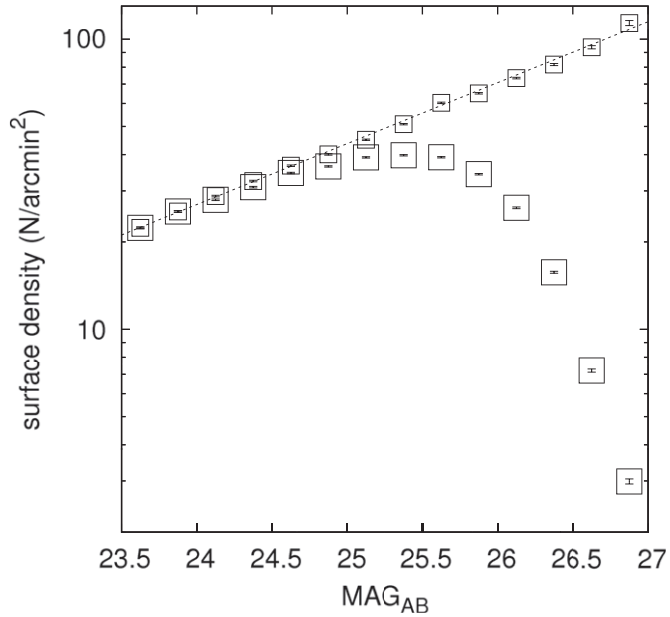

Figure 2. Surface density vs. TENIS *J*-band magnitude plot. The surface density is measured by selecting sources using SExtractor. The large open box indicates the surface density for each magnitude bin. The small open box indicates the surface density for each magnitude bin after the completeness correction. The dotted line is the best fit of the surface density after the completeness correction.

finding. This procedure was run 1000 times to deliver the detection rate of these artificial sources in each magnitude bin, i.e., the completeness. Figure 2 shows that the surface density versus apparent magnitude of the TENIS *J* data. The completeness corrected surface density is used in our analyses later.

2.2. Ancillary Data

We incorporated data from several ECDFS surveys at different wavelengths to perform our analyses. To measure accurate colors for the color selection, we processed the images from the ancillary data to generate new images that are pixel-to-pixel matched to the TENIS images. For the space-based optical images, we also matched their Point Spread Functions (PSFs) to the TENIS data to ensure better color measurements. In this subsection, we describe how we processed the ancillary data and measured fluxes.

2.2.1. MUSYC Data

The MUSYC team has released its deep optical and near-infrared images in the ECDFS. To improve the quality of the photometric redshifts, which will help eliminate foreground contaminations in our study, we included the MUSYC optical data in our analyses. We resampled the MUSYC images in U, $U38$, B, V, R, I, z, and O_3 to match the TENIS J image, and then used the double-image mode of SExtractor with "FLUX_AUTO" to generate a TENIS *J*-selected MUSYC photometric catalog. The zero-point calibration was done by matching the fluxes with those in the published BVR-selected MUSYC catalog (Gawiser et al. 2006). The flux errors of the MUSYC photometry were calibrated using the method described in Section 2.1.4.

2.2.2. GEMS ACS Data

The GEMS project (Rix et al. 2004; Caldwell et al. 2008) provides deep *HST* ACS images with the $F606W$ and $F850LP$ filters in the ECDFS, except some small areas close to bright objects. The 5σ limiting magnitudes for point sources are 28.4 and 27.1 for $F606W$ and $F850LP$, respectively. We mosaicked the public GEMS ACS images and then resampled the images to match the TENIS *J* image. The PSFs of the ACS images are very small compared to the PSFs of the WIRCam images. To derive better color measurements between the ACS filters and *J*, we applied a smoothing kernel to the ACS images to match their PSFs to that of the TENIS *J* image. We then repeated the same procedure as what we did for the MUSYC data to deliver the *J*-selected GEMS photometric catalog with calibrated flux errors.

2.2.3. SIMPLE IRAC Data

The SIMPLE project (Damen et al. 2011) provides deep IRAC observations covering the entire ECDFS with the $10' \times 15'$ GOODS-S IRAC mosaics in its center (Dickinson et al. 2003). We mosaicked the SIMPLE images and resampled them to match the TENIS *J* image. For the flux measurement, however, we could not use SExtractor in the double-image mode with the "FLUX_AUTO" option to generate the *J*-selected IRAC photometric catalog, since the PSFs of IRAC images are about 1.″5–2.″0 arcsec, which are much larger than that of the TENIS *J* image. If we were to do this, the IRAC fluxes would be seriously underestimated as SExtractor uses the aperture size estimated from the reference image (TENIS *J* image) to measure the fluxes on the target image (SIMPLE IRAC images).

One can use SExtractor in the double-image mode with the standard aperture photometry to measure the IRAC fluxes, and then apply the aperture correction values provided in the IRAC data handbook (Chapter 5, Table 5.7) to derive the estimated IRAC total fluxes. However, due to the very large PSFs of IRAC images, using simple aperture photometry to measure the fluxes of deep IRAC images in a relatively crowded field like the ECDFS has serious confusion issues and the local background estimation used in aperture photometry can be easily affected by neighboring objects. We note that the accuracy of the IRAC photometry is critical in our analyses (see Section 3), requiring an alternative method to estimate the IRAC fluxes properly.

Many intensive efforts have gone into developing methods for estimating fluxes in an image with a large PSF (image1, hereafter). The most recent method relies on utilizing the morphological information from a high-quality image in another band (image2, hereafter; e.g., Grazian et al. 2006; Laidler et al. 2007; Wang et al. 2010; McLure et al. 2011). By assuming the intrinsic morphology of objects are identical in the two wavelengths (i.e., no color gradient from its center to edge), one is able to use the PSF of image2 to deconvolve that image, and then convolve the deconvolved image2 with the PSF of image1. The scaling factor that needs to be applied to match the peak values between an object in image2 and the same object in the processed image1 is the flux ratio (color) of that object. The assumption that there is no color gradient, however, does not always stand. We have therefore developed a new method that is quite different from what has been used, but is very similar to the traditional CLEAN deconvolution in radio imaging.

We used the TENIS *J* image as a prior image (i.e., image2) to estimate the fluxes in the IRAC images (i.e., image1). The segmentation map of the TENIS *J* image generated by SExtractor with a 0.7σ threshold preserves the information of what pixels are attributed to each object, and it provides the positional and shape/boundary information of each object when deconvolving the IRAC images. We only used the boundary information rather than the full morphological information adopted

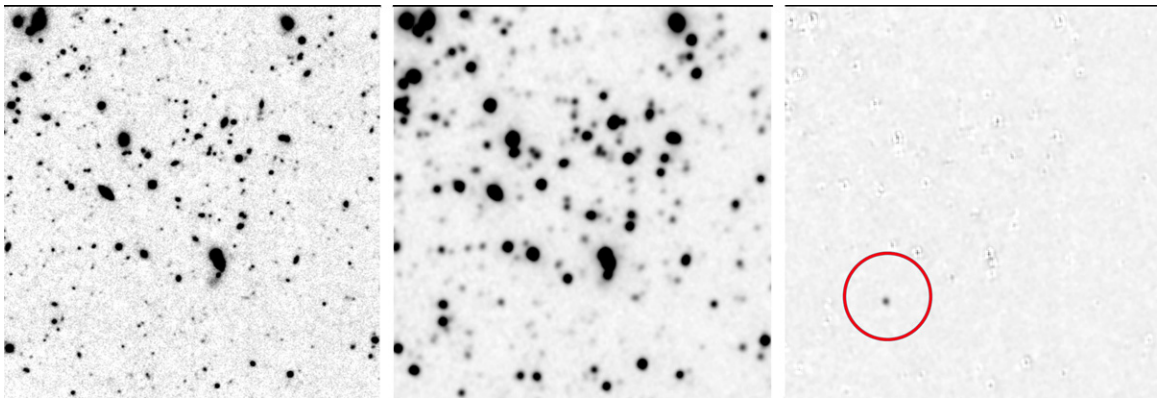

Figure 3. These three panels show the deconvolution quality of the IRAC images. A small region of the TENIS *J* image, the SIMPLE 3.6 μm image, and the residual SIMPLE 3.6 μm image are shown in the left, middle, and right panels. The region of each panel is $135'' \times 135''$. North is up and east is to the left. The brightness and contrast of the three panels are exactly the same. The clean residual image in the right panel shows that the deconvolution works very well. The unsubtracted object marked by the red circle in the right panel is an IRAC-bright source but that is not detected in *J*.

(A color version of this figure is available in the online journal.)

in previous works. The boundary information introduced with the segmentation map is often called the "CLEAN window" in radio image. The IRAC PSFs were generated using bright isolated IRAC point sources in each IRAC channel. The size of the PSF images is $1' \times 1'$. Due to the non-spherical IRAC PSF and different orientations of *Spitzer* in the observing epochs for GOODS-S and SIMPLE, the PSFs of the stacked IRAC image in GOODS-S region is very different from those in the extended area. We tried to use the PSF generated from the SIMPLE data to deconvolve the GOODS-S region and found that the fluctuation of the residual image (see the next paragraph for details of the residual image) is five times larger (i.e., $\sim$1.7 mag worse in limiting magnitude) as compared to the result using the PSF generated from the GOODS-S data itself. We therefore generated an individual PSF for each region and deconvolved the two regions separately.

The deconvolution process always starts at the pixel with the highest value measured within a 9 pixel aperture in diameter ($F_{\rm AP9}$, hereafter), and this pixel must have been registered to one object in the *J* segmentation map. Since the SIMPLE image ($\sim$0.″6 pixel^{-1}) has been resampled to match the TENIS *J*-band image ($\sim$0.″3 pixel^{-1}), simply moving a window (i.e., $F_{\rm AP9}$) across the SIMPLE image to find the location of a peak is very similar to do a sub-pixel centering. Once this pixel is found, we subtracted a scaled PSF from the surrounding $1' \times 1'$ area centered on this pixel. The ratio of the subtracted flux depends on $F_{\rm AP9}$; if $F_{\rm AP9}$ is greater than 5σ, then 0.1% of the flux was subtracted. If $F_{\rm AP9}$ is less than 5σ, then 100% of the flux was subtracted. The subtraction ratio that we use (0.1%) is much smaller than the values that most deconvolution/clean algorithms usually use (10%). We found that a subtraction ratio of 10% for our deconvolution process sometimes produces much worse results especially for bright extended sources because our algorithm is less restricted; 0.1% is the value that has a good balance between performance and quality. The subtracted flux ($F_{\rm SUB}$) was summed and registered to a certain reference object according to the *J* segmentation map. After the subtraction, the deconvolution process is repeated on the subtracted image, until there was no pixel with $F_{\rm AP9}$ higher than 1.5σ. We note that the concept of the deconvolution here is identical to that of CLEAN in radio imaging. At the end of the deconvolution process, the $F_{\rm SUB}$ for each object is the flux measurement of that object, and the final subtracted image is the residual map. The latter allows us to check the quality of the deconvolution, and it is also used for estimating accurate photometric errors. The flux error of each object was calculated based on the fluctuation of the local area around that object in the residual map. Any imperfection of the PSF would cause larger fluctuation in the residual map, and that was taken into account by the flux error calculation.

We demonstrate the performance of this method in Figure 3. A small region of the TENIS *J* image, the SIMPLE 3.6 μm image, and the residual SIMPLE 3.6 μm image are shown in the left, middle, and right panels. The brightness and contrast of the three panels are exactly the same. By comparing the SIMPLE 3.6 μm image to the TENIS *J* image, one can see that many objects in the most dense area are mixed together in the 3.6 μm image while they are still well separated in the TENIS *J* image. After processing the 3.6 μm image using the method described above, the residual image as shown in the right panel of Figure 3 shows that the deconvolution works very well. Sources left in the residual image are objects detected in the IRAC images but not the TENIS *J* image. An example is the object sitting at the center of the red circle in the right panel of Figure 3. This is a bonus of the deconvolution method.

Figure 4 shows a comparison of IRAC photometry using the above-mentioned deconvolution method against that using the SExtractor with FLUX_AUTO. As can be seen, the results of two photometric methods agree with each other for bright objects, but the scatter between the two measurements increases for fainter objects. This is because the flux measurements of faint objects are much more easily affected by neighboring objects, coupled with the fact that fainter objects have higher mean surface number densities. Some bright sources have >0.1 mag differences between their deconvolution and auto magnitudes. According to the flags provided by SExtractor, more than 80% of objects brighter than 20 mag are seriously blended with their neighbors. We also confirmed that all the objects having large differences between their deconvolution and auto magnitudes are blended with their neighbors as shown in their flags. The deconvolution method can deliver more accurate flux estimation for faint sources in the IRAC images, which is an important factor in our selection criterion for $z > 7$ objects (see Section 3). A more detailed description of the deconvolution method we used to estimate the IRAC fluxes is described in B.-C. Hsieh et al. (in preparation).

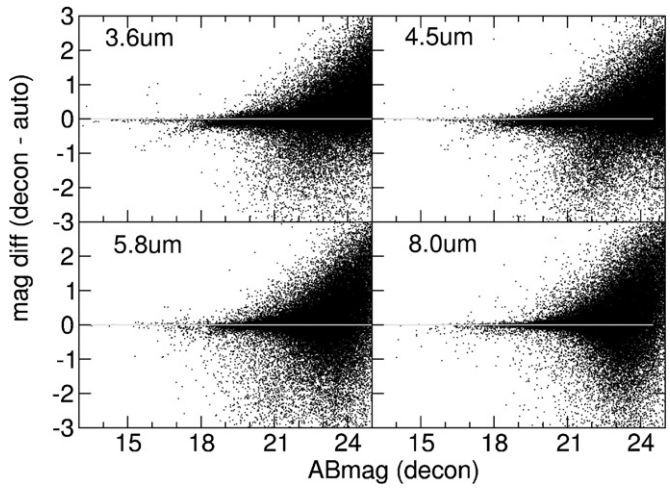

Figure 4. Comparison of the IRAC photometry using difference methods. The differences between the magnitudes using the deconvolution method (decon) and that using the SExtractor with FLUX_AUTO (auto) are shown. It shows that the photometry using two different methods are consistent for bright objects but the scatter between the two measurements increases for fainter objects.

Table 1
5σ Limiting Magnitudes for Point Sources in the *J*-selected Master Catalog

Band	5σ Limiting Magnitude
MUSYC *U*	26.44[a]
MUSYC *U*38	26.34[a]
MUSYC *B*	27.21[a]
MUSYC *V*	26.85[a]
MUSYC *R*	26.80[a]
MUSYC *I*	25.06[a]
MUSYC *z*	24.29[a]
MUSYC *O*3	25.88[a]
GEMS ACS *F606W*	26.80[b]
GEMS ACS *F850LP*	25.72[b]
TENIS *J*	25.57
TENIS K_s	24.95
IRAC 3.6 μm	25.82
IRAC 4.5 μm	25.75
IRAC 5.8 μm	23.77
IRAC 8.0 μm	23.62

Notes.
[a] The MUSYC limiting magnitudes in this table are deeper than those in Gawiser et al. (2006) and Taylor et al. (2009) because we use a smaller aperture size.
[b] The GEMS limiting magnitudes in this table are shallower than those in Rix et al. (2004) and Caldwell et al. (2008) because we use a much larger aperture size. See the text for details.

2.3. *J*-selected Master Catalog

We combined all the data described in this section and generated a 16 band *J*-selected master catalog containing 114 K objects. The 5σ limiting magnitude for point sources in each band is shown in Table 1. For the MUSYC, GEMS, and TENIS data, the values were derived using an 1.″0 aperture in diameter with aperture and noise correlation correction. According to Rix et al. (2004) and Caldwell et al. (2008), the 5σ limiting magnitudes for the GEMS $F606W$ and $F850LP$ are 28.53 and 27.27, which are much deeper than those listed in Table 1, because the aperture size that they use is ∼0.″1 in diameter, which is 10 times smaller as compared to ours. For the SIMPLE data, the aperture we used in the IRAC deconvolution process is a 9 pixel window, which mimics a 3.″0 aperture in diameter for point sources. The IRAC limiting magnitudes in Table 1, which are the medium values derived using point sources with 5σ detections in both SIMPLE and GOODS-S IRAC data. The values are different from those listed in Damen et al. (2011) because of the different methodologies. More details are provided in the TENIS catalog paper (B.-C. Hsieh et al., in preparation). This master catalog is used to select our $z > 7$ sample.

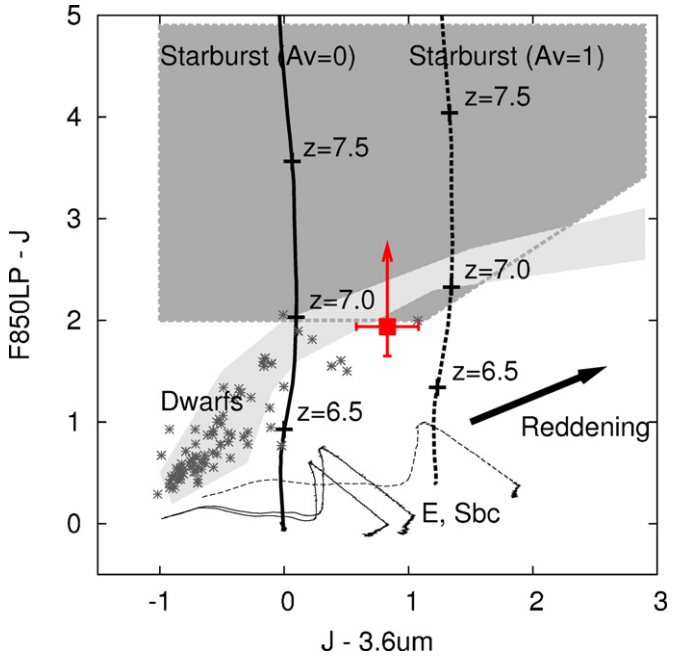

Figure 5. Selection criterion in $J - 3.6\,\mu$m vs. $F850LP - J$ diagram. The thick solid line indicates LBGs at $z > 5.0$ and the thick dotted line indicates LBGs with $Av = 1$ at $z > 5.0$ The two thin solid lines indicate early-type and late-type galaxies at $z < 5.0$, and the thin dotted line indicates late-type galaxies with $Av = 1$ at $z < 5.0$. The black arrow shows the reddening direction. The dark gray area represents the selection criteria of Equation (1) while the light gray area indicates where the Galactic cool stars are, which are estimated using the AMES-dusty model (Allard et al. 2001). The observed M and L dwarfs from IRTF Library are plotted with dark star signs. The red dot indicates the candidate that we find (see Section 4 for details). This figure shows that although the selection criteria can pick up LBGs at $z > 7$ and avoid low-z galaxies with any level of reddening, some L dwarf stars could still be selected as well.
(A color version of this figure is available in the online journal.)

3. CANDIDATE SELECTION

3.1. Color Criterion

For z-dropout studies, the most important issue is to eliminate contaminations from low-z galaxies and Galactic cool stars. Most previous studies make great efforts to estimate the contamination rates, which are not negligible. The accuracies and uncertainties of these estimates, however, are unknown; the best way to deal with the contaminations is to eliminate them in the first place as far as possible. The IRAC photometry provide a good solution to this issue and we discuss how to utilize the IRAC photometry to select a relatively pure sample in this subsection.

Galaxies at different redshifts in a $J - 3.6\,\mu$m versus $F850LP - J$ diagram are shown in Figure 5. The GALAXEV template (Bruzual & Charlot 2003) is used to generate this plot. LBGs at $z > 5$, late-type, and early-type galaxies at $z < 5$ with different extinctions are plotted. Most of the previous z-dropout studies use a simple color cut (e.g., $z - J > 2.0$) to select $z > 7$ objects. However, as shown in Figure 5, heavily reddened low-z galaxies would have very red $z - J$ colors, and the $z - J$ color

of a late-type galaxy with $Av > 3$ would be very similar to that of $z > 7$ objects ($z - J > 2$). Our two-color criteria in the $J-3.6\,\mu$m and $F850LP-J$ space, however, greatly minimizes this issue. The selection criterion are accordingly

$$\begin{aligned} &F850LP - J > 2.0, \\ &J - 3.6\,\mu\text{m} > -1.0, \\ &F850LP - J > 0.8 \times (J - 3.6\,\mu\text{m}) + 1.1, \end{aligned} \quad (1)$$

as shown by the dark gray area in Figure 5. The third criterion is closely parallel to the reddening direction of low-z galaxies, and therefore greatly reduces the contamination rate from low-z galaxies.

Although contamination by low-z galaxies can be effectively dealt with using the criteria defined in Equation (1), contamination by Galactic cool stars can still be problematic. We use the AMES-dusty dwarf star template (Allard et al. 2001) to estimate the distribution of M, L, and T dwarfs in Figure 5, which is plotted as a light gray area. The observed M and L dwarfs from IRTF Library[8] are also shown as dark star signs. We note that there is an overlapped region between our selection criteria (dark gray area) and the dwarf distribution (light gray area). According to the AMES-dusty template, dwarfs in the overlapped region are L dwarfs with effective temperatures between 1700 K and 1900 K. Therefore, we need to make another criterion to discriminate against very cool dwarf stars.

Fortunately, the IRAC colors of dwarf stars are very different from those of high-z galaxies. Therefore, we can minimize the contamination issue from Galactic cool stars by adding another selection criterion:

$$3.6\,\mu\text{m} - 5.8\,\mu\text{m} > 0.12 \times (J - 3.6\,\mu\text{m}) - 0.4. \quad (2)$$

Figure 6 shows how this additional criterion works. The solid and dashed lines indicate starburst galaxies at $z = 5$–10 with $A_V = 0$ and $A_V = 1$, respectively. The arrow indicates the reddening direction. The dark gray area shows the selection criteria for high-z galaxies while the light gray area shows the region occupied by dwarf stars as computed using the AMES-dusty (Allard et al. 2001) model. In Figure 6, high-z galaxies and dwarf stars are well separated, demonstrating that IRAC colors can break the color degeneracy between high-z galaxies and dwarf stars in the optical and near-infrared bands.

To improve the quality of the candidate selection, additional criteria are added to eliminate low-z galaxies that satisfy the above selection criterion because of photometric errors. First, all candidates must have more than 3σ detection in the WIRCam J band. Second, all candidates must have fluxes lower than 1.5σ in optical bands bluer than $F850LP$. We also stack all the optical images (except the $F850LP$ and MUSYC z bands as objects at $z > 7$ may still be detected in z bands) to generate an ultra-deep optical image. McLure et al. (2011) have found that some previously published z-dropout candidates actually have counterparts in ultra-deep stacked optical images that are just contaminations. The ultra-deep stacked optical image therefore allows us to check if some contaminations cannot be detected in our single optical bands because of insufficient sensitivity. We generate two different stacked optical images: one is averaged from MUSYC $U, U38, B, V, R, I$, and GEMS ACS $F606W$ (7 filters); the other is averaged from just red filters (MUSYC V, R, I, and GEMS ACS $F606W$). The former provides the deepest stacked optical image while the latter is optimized for detecting faint red objects. At this stage, 143 objects satisfy all the color criteria.

[8] http://irtfweb.ifa.hawaii.edu/~spex/IRTF_Spectral_Library/

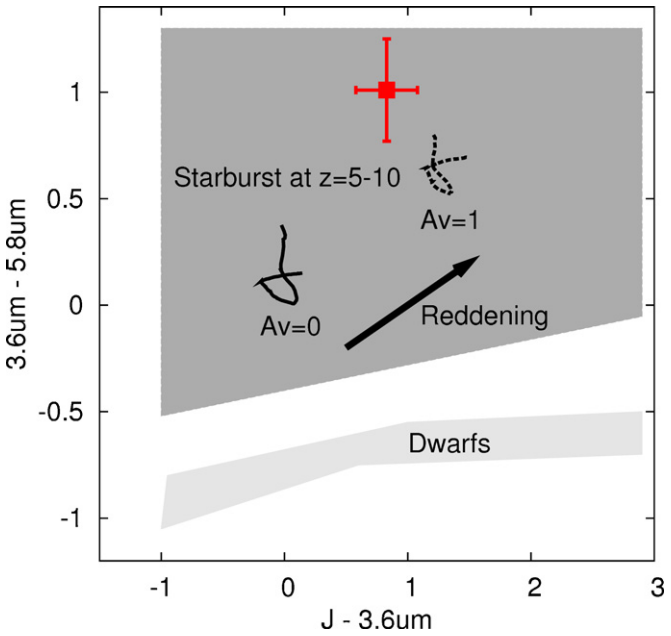

Figure 6. IRAC color–color diagram for high-z galaxies and dwarf stars. The solid line and dashed line indicate starburst galaxies at $z = 5$–10 with $A_V = 0$ and $A_V = 1$, respectively. The arrow indicates the reddening direction. The dark gray area shows the selection criteria for high-z galaxies while the light gray area shows where the dwarf stars are. The red dot indicates the candidate that we find (see Section 4 for details). According to this figure, using IRAC colors can successfully break the color degeneracy between high-z galaxies and dwarfs in optical and near-infrared bands.

(A color version of this figure is available in the online journal.)

3.2. Photometric Redshift Criterion

Although the two color–color selection criteria are very robust for picking up $z > 7$ objects, contaminations can still be present because of photometric errors and transients. Photometric redshift can help to further reduce these issues. It utilizes all the data (16 bands) rather than just the four filters used in our color–color selections, so it is less affected by photometric errors and transients. We use the EAZY code (Brammer et al. 2008) to estimate the photometric redshift of our candidates. We allow a 5% systematic flux error for each band to take into account the systematic errors caused by the fact that for a given object we are not missing the same fraction of light in different passbands that have very different spatial resolutions. To minimize the bias effect of the photometric redshift estimation due to different fitting templates, we use three different templates to run the EAZY code, thus obtaining three photometric redshifts for each candidate. The three templates used are CWW+KIN, default EAZY v1.0, and PÉGASE. The CWW+KIN template is the CWW empirical template (Coleman et al. 1980) with the extension prescribed by Kinney et al. (1996). The default EAZY v1.0 template is generated using the Blanton & Roweis (2007) algorithm with the PÉGASE models and calibrated using semianalytic models, plus an additional young and dusty template. The PÉGASE template is from Fioc & Rocca-Volmerange (1997).

Yan et al. (2004) have found that many IRAC-selected extremely red objects (IERO) with very high photometric redshifts are actually galaxies at $z < 2$ possessing two different

Table 2
Magnitudes of TENIS-ZD1

U	B	R	$F606W$	$F850LP$	J	K_s	3.6 μm	4.5 μm	5.8 μm	8.0 μm
>28.28	>28.85	>28.31	>28.18	>27.05	25.12 ± .23	24.94 ± .34	24.29 ± .10	23.79 ± .06	23.28 ± .22	23.58 ± .40

stellar populations. The EAZY code can fit data with multiple stellar populations simultaneously. For an IERO or similar object, using this function helps to break the degeneracy of high and low redshifts in the template fitting. We use this multiple population fitting function when employing the CWW+KIN and default EAZY v1.0 templates. The documentation on the PÉGASE template suggests that this template works better in the single population fitting mode, and so we decided not to use the multiple population fitting function with the PÉGASE template.

We compile a new list of candidates according to their photometric redshifts. We pick up an object with a photometric redshift between 6.0 and 9.0, and the lower limit of its photometric redshift at 68% confidence level must be greater than 3.0. Since there are three different photometric redshifts for each object, all three photometric redshifts for a chosen candidate must meet the selection criterion simultaneously. We then assign the photometric redshift with the smallest best-fitted χ^2 as the redshift of each candidate. Applying the photometric redshift criterion left 22 objects in our candidate list.

3.3. Cleaning the Sample

All the previous selection criteria rely entirely on photometry (including the photometric redshift estimation). Photometric measurements, however, can be easily affected by CCD bleeding, satellite tracks, diffraction spikes of bright stars, etc., which will also affect the performance of the selection criteria we use. To eliminate these false-detection cases, we visually check the images of every bands for all the 22 remaining candidates and remove 2 affected objects from the list. In addition, objects detected in 24 μm, X-ray, and 1.4 GHz are also omitted since they are very unlikely to be at high z. There are three objects rejected at this stage.

Although we use a color selection criterion in the $J - 3.6\,\mu$m versus 3.6–5.8 μm space to discriminate against Galactic cool stars, this criterion does not work well for some objects which are very faint in 3.6 μm and 5.8 μm. This increases the contamination rate in the candidate selection because the uncertainties in their colors make them spill over into the selection region. To deal with this issue, we perform the SED fitting for the candidates using the AMES-dusty dwarf star template. We reason that an SED fitting would provide better information about the spectral type of an object as it uses the photometry from all the bands as compared to a pure color selection. We reject objects if they have similar or even smaller minimum χ^2 with the AMES-dusty template as compared to those with the galaxy templates. Eighteen objects are rejected in this way.

In the end, only one object survives all the criteria imposed. We name this object TENIS-ZD1. We show its thumbnails in Figure 7 and summarize its photometric results in Table 2. The listed detection limits for the optical bands are 1σ values, and the size of the Kron aperture used for TENIS-ZD1 is $3\farcs2 \times 1\farcs7$ (major and minor axes) according to the output of SExtractor. The FWHM of TENIS-ZD1 in J provided by a Gaussian fitting is $2\farcs3 \pm 0\farcs46$, demonstrating that it is an extended object

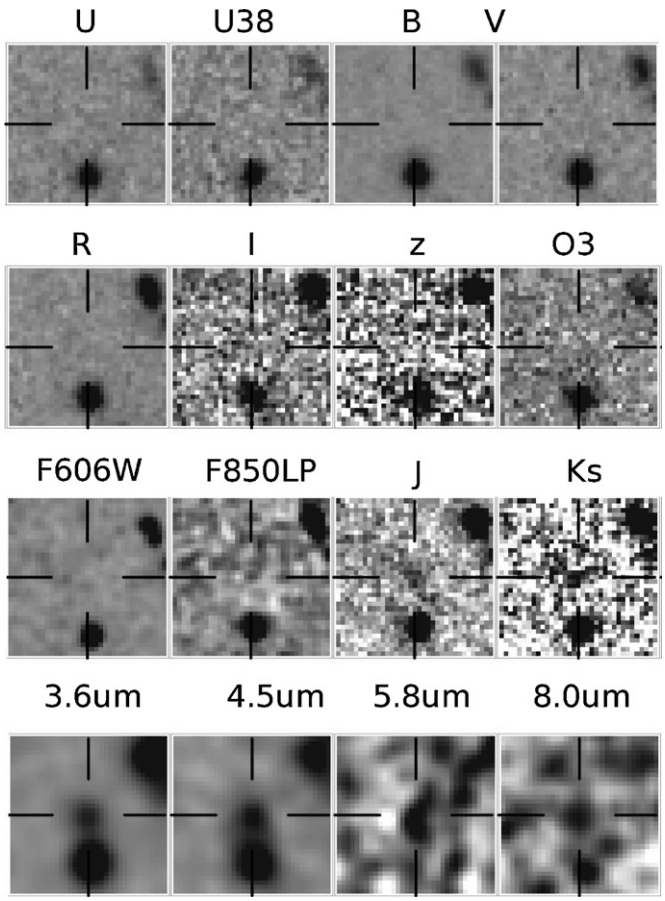

Figure 7. Thumbnail images for TENIS-ZD1. The region of each image is $10'' \times 10''$. North is up and east is to the left. TENIS-ZD1 is not detected in all the optical bands and detected in all the WIRCam and IRAC images.

(and hence not a star). The ultra-deep stacked optical images are also shown in Figure 8 to show that TENIS-ZD1 is not detected in both ultra-deep optical images. As we mentioned in Section 2.2.3, accurate IRAC flux measurements are essential for picking up our candidates. Figure 7 shows that TENIS-ZD1 has a bright close neighbor with a separation of just $3''$. Therefore, the IRAC photometry of TENIS-ZD1 measured using a typical aperture photometry method would be seriously affected by this bright neighbor. In Section 2.2.3 we describe the deconvolution method that we use to derive IRAC fluxes, and Figure 9 shows a comparison between the original IRAC images around TENIS-ZD1, the IRAC images with TENIS-ZD1 but without all the J-band detected neighbors, and the IRAC residual images. It demonstrates that TENIS-ZD1 is well deconvolved in the IRAC images and the photometric effect of its bright neighbor is minimized. The photometric redshift of TENIS-ZD1 estimated by EAZY is $7.822^{+1.095}_{-0.725}$, with a reduced $\chi^2 = 1.15$. The best-fitted templates and the χ^2 versus redshift plots are shown in Figure 10. We also fit an active galactic nucleus (AGN)/quasar template (Polletta et al. 2007) and find a best-fit redshift of $7.069^{+0.398}_{-0.411}$. However, its χ^2 is 6.50, which

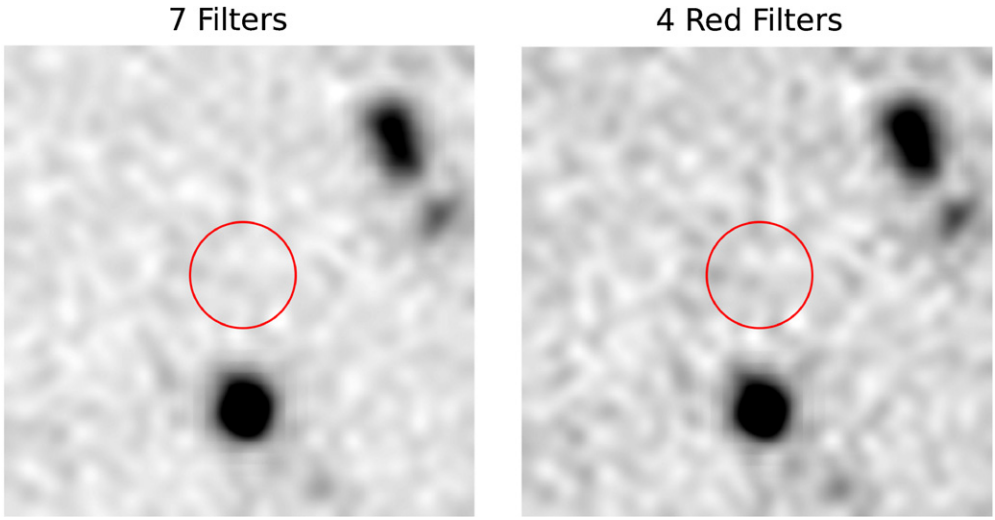

Figure 8. Ultra-deep stacked optical images for TENIS-ZD1. The left-hand image is averaged using MUSYC U, $U38$, B, V, R, I, and GEMS ACS $F606W$ images (seven filters). The right-hand image is combined from MUSYC V, R, I, and GEMS ACS $F606W$ images (four red filters). The region of each image is $12'' \times 12''$. North is up and east is to the left. The details of the ultra-deep stacked optical images are in Section 3.3. The red circle indicates the location of TENIS-ZD1 in the J image. According to these two images, the optical flux of TENIS-ZD1 is below the detection limit even in ultra-deep optical images.

(A color version of this figure is available in the online journal.)

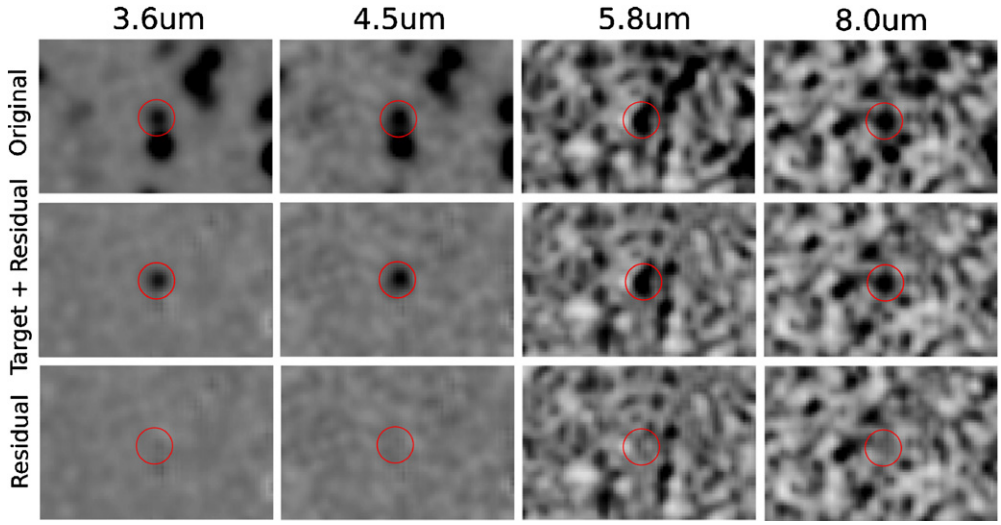

Figure 9. IRAC residual images of TENIS-ZD1. Images from left to right indicate images in IRAC 3.6 μm, 4.5 μm, 5.8 μm, and 8.0 μm. The upper images are the original images of IRAC channels. The middle ones are the images after subtracting all the neighbors (except the target) detected in J using the deconvolution method. The lower ones are the residual images after subtracting all the objects detected in J. The red circle indicates the location of TENIS-ZD1 in the J image. The region of each image is $25'' \times 15''$. North is up and east is to the left. By comparing these three images, they show that TENIS-ZD1 and its bright close neighbor are well deconvolved and well deblended, which suggests that the IRAC flux measurement effect of TENIS-ZD1 due to the bright close neighbor is minimized.

(A color version of this figure is available in the online journal.)

is higher than that of the galaxy fit. Although an AGN is not completely ruled out, the fit favors a galaxy.

4. CONTAMINATION

In this section we discuss the contaminations in our analysis. Ouchi et al. (2009; Ouchi09 hereafter) lists all the possible sources of contamination for z-dropout studies. Here we follow the same items as in Ouchi09 to check the contaminations in our study.

1. *Spurious sources.* One of the selection criterion of our $z > 7$ sample is that the objects must have more than 3σ detections in J, and TENIS-ZD1 has a 4.3σ detection in J. Statistically, an object with a 4.3σ detection is very unlikely a spurious source. As an additional check, we stack the images taken in 07B and 08B separately and generate two mosaic images for the two different semesters. We then measure fluxes of objects in each image using the SExtractor in the double-image mode, by using the J-band master image (07B+08B) for the source detection. The magnitude of TENIS-ZD1 in 07B is 25.03 ± 0.29, while that in 08B is 25.13 ± 0.24. According to the fluxes of TENIS-ZD1 in both semesters, it was well detected in the two epochs. Furthermore, TENIS-ZD1 has counterparts in K_s and IRAC images. All the above evidences suggest that TENIS-ZD1 is not a spurious source.
2. *Transients.* We repeat what we did for checking spurious sources. As we mentioned above, the flux of TENIS-ZD1 in 07B is 25.03 ± 0.29, and that in 08B is 25.13 ± 0.24. The magnitude change between the two epochs is only

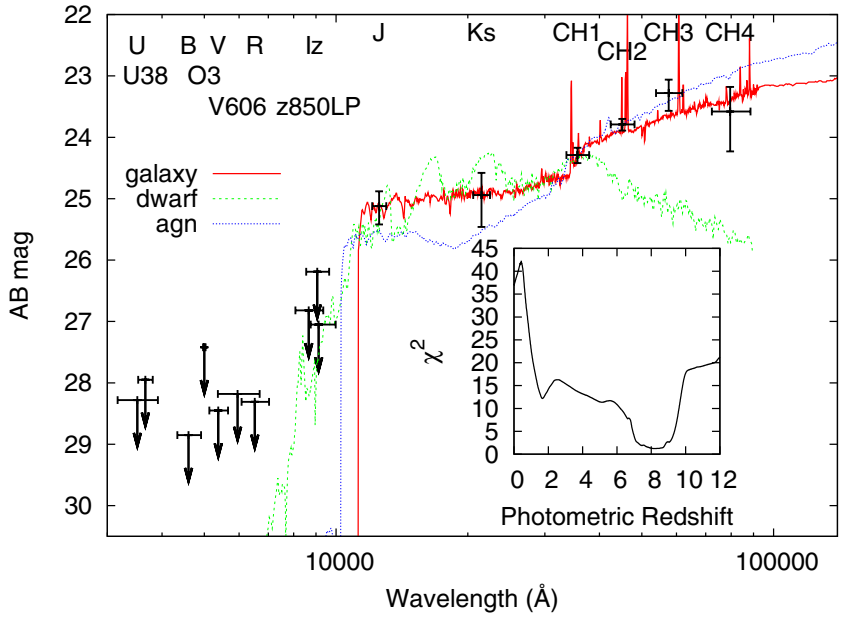

Figure 10. Best-fitted SED and the χ^2 vs. redshift plot. The black data points indicate the AB magnitudes of TENIS-ZD1 in 16 bands. The red, green, and blue lines indicate the best-fitted templates of galaxy, dwarf star, and AGN/quasar, respectively. The χ^2 plot for the best-fitted galaxy template shows that the photometric redshift fitting of TENIS-ZD1 has a very low χ^2 from $z_{\rm phot} = 7.0$ to $z_{\rm phot} = 9.0$, while the weighted $z_{\rm phot}$ is 7.8.

(A color version of this figure is available in the online journal.)

$\sim$0.1 mag, corresponding to a $\sim$10% flux variation. Furthermore, TENIS-ZD1 did not move between the TENIS J-band (07B+08B), K_s-band (09B+10B), and IRAC images, which shows that TENIS-ZD1 is not a slow-moving solar system object. Therefore, we conclude that TENIS-ZD1 is not a transient.

3. *Low-z galaxies.* Our selection criteria avoid selecting galaxies at $z < 6$. However, colors of some low-z galaxies could also meet the selection criteria due to photometric errors. We therefore discuss the possibility of that TENIS-ZD1 is a low-z galaxy. The red data point in Figure 5 shows the position of TENIS-ZD1 in the $J - 3.6\,\mu$m versus $F850LP - J$ diagram. According to Figure 5, although TENIS-ZD1 is right on the boundary of our selection criteria, it is actually a lower limit of its $F850LP - J$ color since it has no detection in the $F850LP$ image. TENIS-ZD1 is still far away from the area of low-z galaxies even if we take its error bars into account. Furthermore, although there is a local minimum at $z < 2$ in the photometric redshift χ^2 plot of Figure 10, its χ^2 value is $\sim$12, which is much larger than that at $z \sim 7$–9. However, the color of a dusty type-2 AGN at $z \sim 1.5$ can be very similar to that of a galaxy at $z \sim 7$, which makes it another possible source of low-z contaminants. We derived the expected fluxes at 1.4 GHz, 24 μm, and 2–8 keV for TENIS-ZD1 by assuming a type-2 AGN at $z \sim 1.5$; they are $\sim$1785 uJy (radio-loud case) or $\sim$0.7 uJy (radio-quiet case), $\sim$22 mag (AB), and $6.4 \times 10^{-16} - 3.6 \times 10^{-15}$ erg cm^{-2} s^{-1} for 1.4 GHz, 24 μm, and 2–8 keV, respectively. The 1σ detection limits for the available data at these wavelengths, however, are 8.5 uJy, 21.2 mag (AB), and 6.7×10^{-16} erg cm^{-2} s^{-1} for 1.4 GHz, 24 μm, and 2–8 keV, respectively. Non-detections of TENIS-ZD1 at these wavelengths therefore cannot rule out a dusty radio-quiet type-2 AGN with weak X-ray luminosity at $z \sim 1.5$. Hence, we did another check by doing an SED fitting within a redshift range between 1.0 and 2.0 for TENIS-ZD1 using an AGN/quasar template from Polletta et al. (2007). The best-fitted template is the QSO2 template. According to the fitting result, the expected z-band magnitude is $\sim$26 mag, which should be a 5σ detection in the GEMS $F850LP$ image, but the signal-to-noise ratio of TENIS-ZD1 in the GEMS image is less than 1σ. The best-fitted SED also fails to reproduce the steep color slope between K_s band and 4.5 μm. Furthermore, Figure 13 in Capak et al. (2011) shows that objects at $z \ll 7$ still can match the $z > 7$ selection criteria. The $J - 4.5\,\mu$m color of TENIS-ZD1 is 1.33 ± 0.24, which is outside the color range of any $z \ll 7$ galaxies ($J - 4.5\,\mu$m < 1.0 even for extreme cases). It is therefore extremely difficult to explain TENIS-ZD1's photometric properties using low-z galaxies.

4. *Galactic cool stars.* Although our selection criteria can separate dwarf stars and high-z galaxies (see Figure 6), contaminations from Galactic cool stars can still be present because of photometric errors. The red data point in Figure 6 indicates TENIS-ZD1. According to Figure 6, the 3.6–5.8 μm color of TENIS-ZD1 is too red as compared to that of dwarfs. Moreover, the FWHM of TENIS-ZD1 in the J-band image shows it is an extended source. All these evidences suggest that TENIS-ZD1 is not a Galactic cool star.

5. DISCUSSIONS

5.1. Surface Density

The cumulative surface density of our sample is $\sim 1 \times 10^{-3}$ arcmin^{-2} to $J < 25.1$. According to Figure 4 in Yan et al. (2011; Yan11 hereafter), this value matches that estimated from the LF based on the WFC3 z_{850}-dropout results for $z \sim 7$ galaxies. Yan11 claims that the estimation of the cumulative surface density is applicable over the redshift range of $6.4 < z < 7.7$. In other words, it suggests that such an extremely luminous galaxy with $6.4 < z < 7.7$ can be found in a

$\sim$1000 arcmin^2 survey. Therefore, the discovery of TENIS-ZD1 is statistically predictable based on previous studies using fainter samples.

5.2. UV Luminosity and Star Formation Rate

The EAZY code cannot provide physical properties (e.g., age, stellar mass, etc.) other than photometric redshifts. Therefore, we use the New-Hyperz (Rose et al.[9]) with the GALAXEV templates (Bruzual & Charlot 2003) to estimate the physical properties of TENIS-ZD1. We pass the best-fitted $z_{\rm phot}$ derived by EAZY to New-Hyperz and treat it as a fixed parameter during the template fitting. The extinction model from Calzetti et al. (2000) is used. The best-fitted template ($\chi^2 = 1.38$) shows that TENIS-ZD1 is a starburst galaxy, with an age of only 45M years and a stellar mass of $3.2 \times 10^{10}\,M_\odot$. The extinction is mild, with an $Av = 0.6$. The absolute UV magnitude M_{1600} is -22.35 before the extinction correction. We then derive the extinction-corrected M_{1600}, $M_{1600}^{\rm corr}$, using the following formula:

$$F_{\rm obs} = F_o \times 10^{(-0.4 \times Av \times K_\lambda/4.05)} \quad (3)$$

(Calzetti et al. 2000), where $K_\lambda = K_{1600} = 9.97$, and $Av = 0.6$. The correction value is -1.48 mag and hence $M_{1600}^{\rm corr}$ is -23.83. We then estimate the SFR using the following formula (Madau et al. 1998):

$$\mathrm{SFR} = L_{\rm UV}(\mathrm{erg\,s^{-1}\,Hz^{-1}})/(8 \times 10^{27}). \quad (4)$$

For the extinction-corrected case, the estimated SFR is $\sim$200 $M_\odot$ yr^{-1}, while for the extinction-uncorrected case, the SFR is $\sim$50 $M_\odot$ yr^{-1}.

We try to estimate the number of galaxies at $z > 7$ using the semianalytic simulation result from Guo et al. (2011), which is based on the Millennium Simulations. The result suggests that ONE galaxy at $7 < z < 8$ with a stellar mass greater than $10^{10}\,M_\odot$ can be detected in the TENIS project, which supports the existence of TENIS-ZD1. However, the value of σ_8 used in the Millennium Simulations is 0.9, and the most recent estimate of σ_8 is 0.809 ± 0.024 derived using the *WMAP7* data (Komatsu et al. 2011), which is almost 4σ smaller than that used in the Millennium Simulations. Structure formation would be faster with a larger σ_8 as massive objects can form earlier. It is possible that, with the revised σ_8, the number of galaxies similar to TENIS-ZD1 produced in the Millennium Simulation might be less than one in our survey volume.

There are several massive galaxies at $z \sim 6$ with IRAC detections reported in Yan et al. (2005, 2006) and Eyles et al. (2007). According to their analyses, the stellar masses of these galaxies are about several $10^{10}\,M_\odot$ and their progenitors can be observed at $z \gtrsim 7$. In particular, they point out that the $z \sim 6$ sample strongly indicates that the universe was already forming galaxies as massive as $\sim 10^{10}\,M_\odot$ at $z \gtrsim 7$ and possibly even at $z \sim 20$, which supports the existence of TENIS-ZD1.

Although it is challenging to explain how to accumulate so much material and trigger such violent star formation at $z > 7$ with current cosmological models, the observational results of $z \sim 6$ galaxies suggest the existence of TENIS-ZD1 is reasonable. Therefore bright high-z objects like TENIS-ZD1 can provide an important constraint for developing and modifying models.

[9] http://www.ast.obs-mip.fr/users/roser/hyperz/

5.3. Luminosity Function

Based on the value of M_{1600}, TENIS-ZD1 is an extremely luminous object at $z > 7$. To date, TENIS-ZD1 is brighter than all published $z > 7$ samples except for the sample provided by Capak et al. (2011) (Capak11 hereafter). Hence, TENIS-ZD1 provides a new constraint to the very bright end of the LF at $z > 7$. In order to make an LF plot with TENIS-ZD1, we estimate the effective comoving volume for our analyses using a Monte Carlo simulation which is modified from Ouchi09.

First of all, we generate a mock catalog for LBGs using the starburst template of the GALAXEV model (Bruzual & Charlot 2003) with apparent J magnitudes from 22.0 to 27.0. The surface density versus apparent magnitude relation of the mock catalog follows that of all the objects shown in Figure 2, where we have assumed that LBGs have a similar surface density versus apparent magnitude dependency. The objects are uniformly distributed in the redshift space, and their ages are randomly distributed from 1M years to 500M years. The extinctions of Calzetti et al. (2000) with $Av = 0.0$–2.0 are also applied to simulate bluer and redder LBGs. Dow-Hygelund et al. (2007) show that roughly only one-third of dropout-selected galaxies at $z = 5$–6 have strong Lyα lines with rest-frame equivalent widths $>$20 Å. The fraction might be even lower at $z > 7$ because of the absorption by the intergalactic medium (IGM). We therefore added Lyα emissions with equivalent widths of 20 Å for 25% of the objects. We assume that 50% of the objects have no Lyα emission. For the remaining 25% of the objects, we added Lyα emissions with equivalent widths of 1–20 Å. After taking all of the above-mentioned effects into account, we disturb the photometry of the catalog to match to the real data.

Equations (1) and (2) are applied to the mock catalog to select candidates. We computed the redshift distribution $C(m, z)$ as the ratio between the number of candidates and the input objects in a magnitude bin of $m = 25^{+0.25}_{-0.25}$, and estimated the comoving volume density for a given magnitude bin by using the relation

$$n(m) = \frac{N_{\rm cand}(m) \times F_c(m)}{\int_0^\infty \frac{dV}{dz} C(m, z) dz}, \quad (5)$$

which is similar to Equation (2) in Ouchi09, where $N_{\rm cand}(m)$ is the number of candidates in the given magnitude bin, $F_c(m)$ is the completeness correction, dV/dz is the differential comoving volume for the field size of the ECDFS, and $m = 25$ is the only magnitude bin we used since our candidate is in that magnitude bin. In order to convert the unit of $n(m)$ ($N0.5\,\mathrm{mag^{-1}\,Mpc^{-3}}$) to $N\,\mathrm{mag^{-1}\,Mpc^{-3}}$, a factor of two needs to be applied to $n(m)$. We make the LF plot, including the data from several previous studies, as shown in Figure 11. The LFs provided by Ouchi09 and Yan11 fitted including luminous samples are also plotted. The error of our data point is calculated based on a simple Poissonian uncertainty for an event rate of 1, which is ± 1. On the other hand, the 90% Baysian confidence level for such an event rate (Kraft et al. 1991) would be 0.08–3.93. In either case, our result is consistent with both Ouchi09 and Yan11.

Several papers claim that the LF at $z \sim 7$ decreases from $z \sim 6$ at the bright end (e.g., Mannucci et al. 2007; Castellano et al. 2010; Ouchi et al. 2009; Bouwens et al. 2010a), while Yan11 shows no/very mild evolution. These studies are done using samples with $M_{\rm UV} > -22$ while our sample would provide a better constraint at the very bright end ($M_{\rm UV} < -22$). However, our sample is not sufficient to distinguish between the two cases since our result is consistent with both Ouchi09 and Yan11 within the uncertainties. On the other hand, Capak11

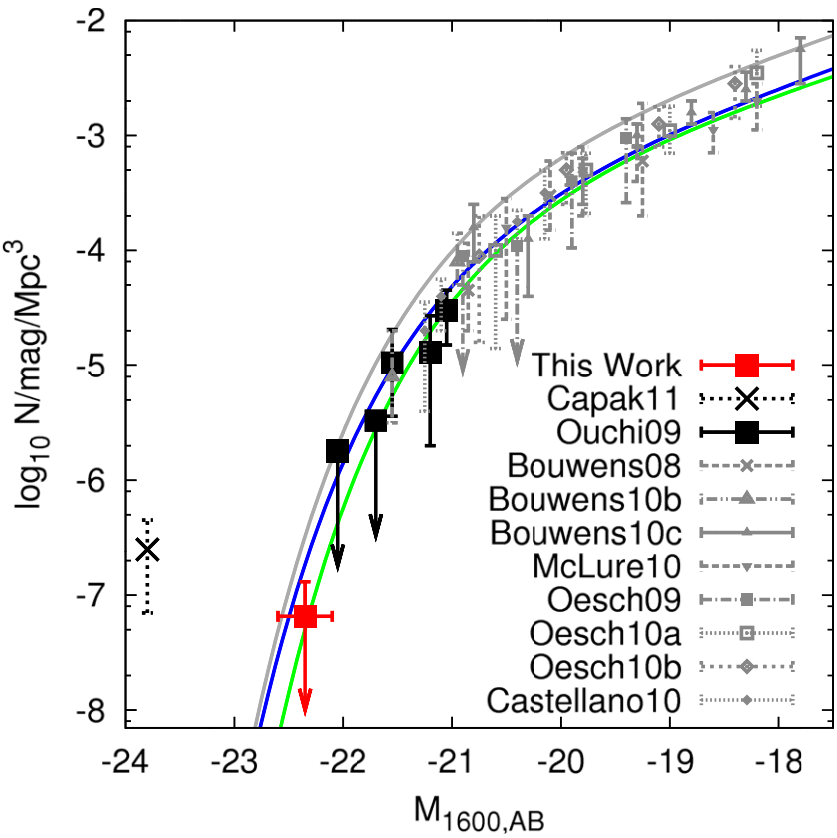

Figure 11. Luminosity function at $z \sim 7$. The red filled square indicates our sample, the black filled square indicates the sample in Ouchi09, and the black cross indicates the sample in Capak11. The other gray data points show the samples from Bouwens et al. (2008, 2010a, 2010c), McLure et al. (2010), Oesch et al. (2009, 2010b, 2010a), and Castellano et al. (2010). The blue solid line and green solid line represent the LF at $z \sim 7$ provided by Yan11 and Ouchi09, respectively. The LF at $z \sim 6$ in Bouwens et al. (2007) is also shown as the gray solid line. Our result is consistent with both Ouchi09 and Yan11.

(A color version of this figure is available in the online journal.)

shows a $z \sim 7$ LF with a very high bright end, according to a sample even brighter than ours. We note that we use very restricted criteria to select our candidate. While these criteria would eliminate contaminations as much as possible, some objects at $z > 7$ could also be rejected at the same time. From this point of view, the constraint that our sample provides for the LF is a lower limit, and thus we cannot completely rule out the LF from Capak11. Furthermore, cosmic variance can be as high as a factor of 10 since the extremely luminous galaxies are strongly clustered at $z > 5$ (Ouchi et al. 2004; Hildebrandt et al. 2009). It is reasonable that the results based on observations covering less than a few square degrees may show large discrepancies.

6. CONCLUSIONS

The TENIS project provides deep J and K_s images for the ECDFS. We use these data with the other deep surveys in optical and infrared to find $z > 7$ objects. New color criteria with IRAC data for selecting $z > 7$ candidates are used because we find that accurate IRAC photometry provide the key to resolve contamination by low-z galaxies and Galactic dwarf stars. Because the PSFs of IRAC data are much larger than those of the data in the other wavelengths, we introduce a novel deconvolution method to address the confusion in the IRAC images and provide accurate IRAC fluxes. After carefully checking our sample, we found one candidate at $z > 7$, TENIS-ZD1.

The weighted $z_{\rm phot}$ of TENIS-ZD1 is 7.8, with an estimated stellar mass $= 3.2 \times 10^{10}\,M_{\odot}$. The extinction-corrected current SFR of TENIS-ZD1 is $\sim 200\,M_{\odot}$ yr^{-1}, but must have been very much higher in the past. We summarize the results of our sample below: (1) the discovery of TENIS-ZD1 is predictable in an 1000 arcmin^2 survey according to the surface density derived from literatures. (2) Our sample matches to both LFs from Ouchi09 and Yan11. (3) While the existence of TENIS-ZD1 is supported by the observations at $z \sim 6$, it is still hard to explain how such a massive galaxy can form in the early universe based on current cosmological models for structure formation.

In the end, we would like to emphasize that the TENIS project provides the most comprehensive data set possible to address the problem of finding luminous high-z galaxies. Compared with fainter high-z samples, such high-z massive objects like TENIS-ZD1 provide the greatest leverage in testing galaxy formation/evolution models. Such objects are the best candidates for follow-up spectroscopy with large telescopes; at the same time, to minimize wastage of observing times on large telescopes, all efforts must first be made to weed out contaminants. The sizes of the $z \sim 7$ bright samples are very small due to the limited field size of deep near-infrared surveys, and the purity and completeness issues of the dropout technique need to be further investigated. Due to the severe contamination issue of the bright end of the $z \sim 7$ LF, all the studies make great efforts on increasing the purity of their samples; however, all these efforts may also harm the completeness of the samples, which makes the bright end of the $z \sim 7$ LF seriously underestimated.

Hu & Cowie (2006) point out that the bright end of the LF at $z \sim 6$ based on LAE studies is much higher than that based on LBG studies. Capak11 also claims that the bright end of the LF at $z \sim 7$ could be much higher than the results derived using the dropout technique. The bright samples will increase very soon since there will be more and more large field near-infrared surveys. However, simply increasing the bright sample size cannot solve the bias issue. The best way is to confirm their redshifts spectroscopically. Each spectroscopically confirmed object will set a robust lower limit for that luminosity bin of the LF. The *James Webb Space Telescope* (*JWST*) and 30 m class telescopes (e.g., TMT and GMT) will be certainly capable for these confirmation observations. But before the era of *JWST* and 30 m class telescopes comes, the current 10 m class telescopes are still able to perform the observations for objects with $M_{\rm UV} < -21$ as long as strong Lyα lines exist. These spectroscopic observations will provide very important information for inspecting the real performance of the dropout studies at $z > 7$.

We thank the referee for comments that greatly improved the manuscript. We are grateful to the CFHT staff for their help obtaining the data, and H. K. C. Yee and Y. T. Lin for useful discussions. This paper is based on observations obtained with the WIRCam, a joint project of CFHT, Taiwan, Korea, Canada, France, and the Canada–France–Hawaii Telescope (CFHT) which is operated by the National Research Council (NRC) of Canada, the Institute National des Sciences de l'Univers of the Centre National de la Recherche Scientifique of France, and the University of Hawaii. Access to the CFHT was made possible by the Ministry of Education, the National Science Council of Taiwan as part of the Cosmology and Particle Astrophysics (CosPA), the Institute of Astronomy and Astrophysics, Academia Sinica, and National Tsing Hua University, Taiwan. We gratefully acknowledge support from the National Science Council of Taiwan Grant 98-2112-M-001-003-MY2 (W.H.W.), 99-2112-M-001-012-MY3 (W.H.W), and Japanese Government FIRST program (H.K.).

REFERENCES

Allard, F., Hauschildt, P. H., Alexander, D. R., Tamanai, A., & Schweitzer, A. 2001, ApJ, 556, 357
Bertin, E., & Arnouts, S. 1996, A&AS, 117, 393
Blanton, M. R., & Roweis, S. 2007, AJ, 133, 734
Bouwens, R. J., Illingworth, G. D., Bradley, L. D., et al. 2009a, ApJ, 690, 1764
Bouwens, R. J., Illingworth, G. D., Franx, M., & Ford, H. 2007, ApJ, 670, 928
Bouwens, R. J., Illingworth, G. D., Franx, M., & Ford, H. 2008, ApJ, 686, 230
Bouwens, R. J., Illingworth, G. D., Franx, M., et al. 2009b, ApJ, 705, 936
Bouwens, R. J., Illingworth, G. D., González, V., et al. 2010a, ApJ, 725, 1587
Bouwens, R. J., Illingworth, G. D., Oesch, P. A., et al. 2010b, ApJ, 709, L133
Bouwens, R. J., Illingworth, G. D., Oesch, P. A., et al. 2010c, ApJ, 737, 90
Bradley, L. D., Bouwens, R. J., Ford, H. C., et al. 2008, ApJ, 678, 647
Brammer, G. B., van Dokkum, P. G., & Coppi, P. 2008, ApJ, 686, 1503
Bruzual, G., & Charlot, S. 2003, MNRAS, 344, 1000
Bunker, A., Wilkins, S., Ellis, R. S., et al. 2010, MNRAS, 409, 855
Caldwell, J. A. R., McIntosh, D. H., Rix, H.-W., et al. 2008, ApJS, 174, 136
Calzetti, D., Armus, L., Bohlin, R. C., et al. 2000, ApJ, 533, 682
Capak, P., Mobasher, B., Scoville, N. Z., et al. 2011, ApJ, 730, 68
Cardamone, C. N., van Dokkum, P. G., Urry, C. M., et al. 2010, ApJS, 189, 270
Castellano, M., Fontana, A., Boutsia, K., et al. 2010, A&A, 511, 20
Coleman, G. D., Wu, C.-C., & Weedman, D. W. 1980, ApJS, 43, 393
Damen, M., Labbé, I., van Dokkum, P. G., et al. 2011, ApJ, 727, 1
Dickinson, M., et al. FIDEL Team 2007, AAS, 211, 5216
Dickinson, M., Giavalisco, M., GOODS Team, et al. 2003, in Proc. European Southern Observatory and Universitäts-Sternwarte München Workshop, ESO Astrophysics Symposia, The Mass of Galaxies at Low and High Redshift, ed. R. Bender & A. Renzini (Berlin: Springer), 324
Dow-Hygelund, C. C., Holden, B. P., Bouwens, R. J., et al. 2007, ApJ, 660, 47
Eyles, L. P., Bunker, A. J., Ellis, R. S., et al. 2007, MNRAS, 374, 910
Fioc, M., & Rocca-Volmerange, B. 1997, A&A, 326, 950
Gawiser, E., van Dokkum, P. G., Gronwall, C., et al. 2006, ApJ, 642, L13
González, V., Labbé, I., Bouwens, R. J., et al. 2010, ApJ, 713, 115
Grazian, A., Fontana, A., de Santis, C., et al. 2006, A&A, 449, 951
Guo, Q., White, S., Boylan-Kolchin, M., et al. 2011, MNRAS, 413, 101
Henry, A. L., Malkan, M. A., Colbert, J. W., et al. 2007, ApJ, 656, L1
Henry, A. L., Malkan, M. A., Colbert, J. W., et al. 2008, ApJ, 680, L97
Henry, A. L., Siana, B., Malkan, M. A., et al. 2009, ApJ, 697, 1128
Hickey, S., Bunker, A., Jarvis, M. J., Chiu, K., & Boneld, D. 2010, MNRAS, 404, 212
Hildebrandt, H., Pielorz, J., Erben, T., et al. 2009, A&A, 498, 725
Hu, E. M., & Cowie, L. L. 2006, Nature, 440, 1145
Iye, M., Ota, K., Kashikawa, N., et al. 2006, Nature, 443, 186
Kashikawa, N., Shimasaku, K., Malkan, M. A., et al. 2006, ApJ, 648, 7
Kellerman, K. I., Fomalont, E. B., Mainieri, V., et al. 2008, ApJS, 179, 71
Kinney, A. L., Calzetti, D., Bohlin, R. C., et al. 1996, ApJ, 467, 38
Komatsu, E., Smith, K. M., Dunkley, J., et al. 2011, ApJS, 192, 18
Kraft, R. P., Burrows, D. N., & Nousek, J. A. 1991, ApJ, 374, 344
Laidler, V. G., Papovich, C., Grogin, N. A., et al. 2007, PASP, 119, 1325
Lehmer, B. D., Brandt, W. N., Alexander, D. M., et al. 2005, ApJS, 161, 21
Madau, P., Pozzetti, L., & Dickinson, M. 1998, ApJ, 498, 106
Mannucci, F., Buttery, H., Maiolino, R., Marconi, A., & Pozzetti, L. 2007, A&A, 461, 423
Martin, D., Fanson, J., Schiminovich, D., et al. 2005, ApJ, 619, 1
McLure, R. J., Cirasuolo, M., Dunlop, J. S., Foucaud, S., & Almaini, O. 2009, MNRAS, 395, 2196
McLure, R. J., Dunlop, J. S., Cirasuolo, M., et al. 2010, MNRAS, 403, 960
McLure, R. J., Dunlop, J. S., de Ravel, L., et al. 2011, MNRAS, 418, 2074
Oesch, P. A., Bouwens, R. J., Carollo, C. M., et al. 2010a, ApJ, 709, L21
Oesch, P. A., Bouwens, R. J., Illingworth, G. D., et al. 2010b, ApJ, 709, L16
Oesch, P. A., Carollo, C. M., Stiavelli, M., et al. 2009, ApJ, 690, 1350
Ota, K., Iye, M., Kashikawa, N., et al. 2008, ApJ, 677, 12
Ota, K., Iye, M., Kashikawa, N., et al. 2010, ApJ, 722, 803
Ouchi, M., Mobasher, B., Shimasaku, K., et al. 2009, ApJ, 706, 1136
Ouchi, M., Shimasaku, K., Furusawa, H., et al. 2010, ApJ, 723, 869
Ouchi, M., Shimasaku, K., Okamura, S., et al. 2004, ApJ, 611, 685
Polletta, M., Tajer, M., Maraschi, L., et al. 2007, ApJ, 663, 81
Puget, P., Stadler, E., Doyon, R., et al. 2004, Proc. SPIE, 5492, 978
Richard, J., Stark, D. P., Ellis, R. S., et al. 2008, ApJ, 685, 705
Rix, H.-W., Barden, M., Beckwith, S. V. W., et al. 2004, ApJS, 152, 163
Shimasaku, K., Kashikawa, N., Doi, M., et al. 2006, PASJ, 58, 313
Sobral, D., Best, P. N., Geach, J. E., et al. 2009, MNRAS, 398, L68
Stark, D. P., Ellis, R. S., Richard, J., et al. 2007, ApJ, 663, 10
Taniguchi, Y., Ajiki, M., Nagao, T., et al. 2005, PASJ, 57, 165
Taylor, E. N., Franx, M., van Dokkum, P. G., et al. 2009, ApJS, 183, 295
Trenti, M., Bradley, L. D., Stiavelli, M., et al. 2011, ApJ, 727, L39
Trenti, M., Bradley, L. D., Stiavelli, M., et al. 2012, ApJ, 746, 55
Wang, W.-H., Cowie, L. L., Barger, A. J., Keenan, R. C., & Ting, H.-C. 2010, ApJS, 187, 251
Wilkins, S. M., Bunker, A. J., Ellis, R. S., et al. 2010, MNRAS, 403, 938
Wilkins, S. M., Bunker, A. J., Lorenzoni, S., & Caruana, J. 2011, MNRAS, 411, 23
Wolf, C., Dye, S., Kleinheinrich, M., et al. 2001, A&A, 377, 442
Yan, H., Dickinson, M., Eisenhardt, P. R. M., et al. 2004, ApJ, 616, 63
Yan, H., Dickinson, M., Giavalisco, M., et al. 2006, ApJ, 651, 24
Yan, H., Dickinson, M., Stern, D., et al. 2005, ApJ, 634, 109
Yan, H., Yan, L., Zamojski, M. A., et al. 2011, ApJ, 728, 22
Zheng, W., Bradley, L. D., Bouwens, R. J., et al. 2009, ApJ, 697, 1907